Nanoscale Compositional Mapping of Commercial LiNi$_{0.8}$Co$_{0.15}$Al$_{0.05}$O$_2$ Cathodes Using Atom Probe Tomography

Published as part of The Journal of Physical Chemistry virtual special issue "Esther Sans Takeuchi Festschrift".

Pritesh Parikh, Hyeseung Chung, Ethan Vo, Abhik Banerjee, Ying Shirley Meng,* and Arun Devaraj*

Read Online

ACCESS | Metrics & More | Article Recommendations | Supporting Information

ABSTRACT: Nickel-rich cathodes provide improved specific capacity, which leads to higher gravimetric energy density, which, in turn, is critical for electric vehicles. However, poor long-term capacity retention at elevated temperatures/high C rates (the rate of charge and discharge on a battery) stems from material issues: surface phase changes, corrosive side reactions with the electrolyte, ion dissolution, and propagation of cracks. Introducing dopants, developing nanoscale surface coatings, and graded core–shell structures all improved the electrochemical performance of nickel-rich cathodes. However, material-level understanding of the effect of Li composition and distribution in Ni-rich cathodes is limited due to a lack of characterization methods available that can directly image Li at the nanoscale. Hence, it is critical to establish methods such as atom probe tomography (APT) that have both nanometer-scale spatial resolution and high compositional sensitivity to quantitatively analyze battery cathodes. To fully realize its potential as a method for quantitative compositional analysis of commercial Li-ion batteries, we provide a comprehensive description of the challenges in sample preparation and analyze the dependency of the analysis parameters, specifically laser pulse energy on the measured stoichiometry of elements in a high-Ni-content cathode material LiNi$_{0.8}$Co$_{0.15}$Al$_{0.05}$O$_2$ (NCA). Our findings show that the stoichiometry variations cannot be explained by charge–state ratios or Ga implantation damage alone during FIB preparation, indicating that additional factors such as crystallographic orientation may need to be considered to achieve quantitative nanoscale compositional analysis of such battery cathodes using APT.
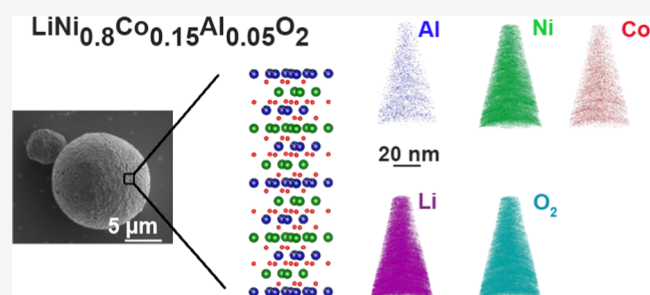
INTRODUCTION

As the push for a green economy takes center stage worldwide, lithium-ion batteries provide a unique opportunity to satisfy energy demands for various market segments. From grid storage, energy tools, and electric vehicles to consumer electronics, continuous R&D efforts for battery materials have provided significant market penetration. As the lithium-ion battery market continues to grow, the need to understand and develop novel materials and solutions also continues to increase. High-Ni-content cathodes based on transition metal oxides (>80% by stoichiometry such as NCA-LiNi$_{0.8}$Co$_{0.15}$Al$_{0.05}$O$_2$ and NMC811-LiNi$_{0.8}$Mn$_{0.1}$Co$_{0.1}$O$_2$) are the preferred cathodes of choice for future development due to their ability to provide higher gravimetric energy density.

However, these cathode materials suffer from long-term capacity retention issues and severe capacity fading either at elevated temperatures or with rapid cycling. Specifically, NMC811-LiNi$_{0.8}$Mn$_{0.1}$Co$_{0.1}$O$_2$ still suffers a host of different issues: [a] heavy Li/Ni intermixing (due to similar ionic radii) that impedes Li transport, [b] side reactions with the electrolyte and formation of an electrochemically inactive surface disordered phases due to highly reactive Ni^{4+}; and [c] formation of microcracks due to anisotropic lattice contractions.[1−6] All these issues can cause local nanoscale changes in the composition and distribution of elements, which ultimately affect the available Li transport channels and capacity retention.[7−9] Moreover, strategies to mitigate these issues typically involve nanoscale coatings (both through solution chemistry[1,10] and atomic layer deposition (ALD)[11]), graded compositions from the surface to bulk within micron-sized particles,[12,13] and doping/substitution at concentrations typically below 1 atomic %.[14]

A quantitative analysis of individual primary and secondary particles as well as the modified particles (from various mitigative strategies) for both elemental composition and uniformity at the nanoscale level can help to better understand Li ionic transport channels to provide the structure–property relationships for batteries. Requirements include enabling quantitative estimates of doping distributions for light elements and imaging the Li distribution in individual cathode particles.
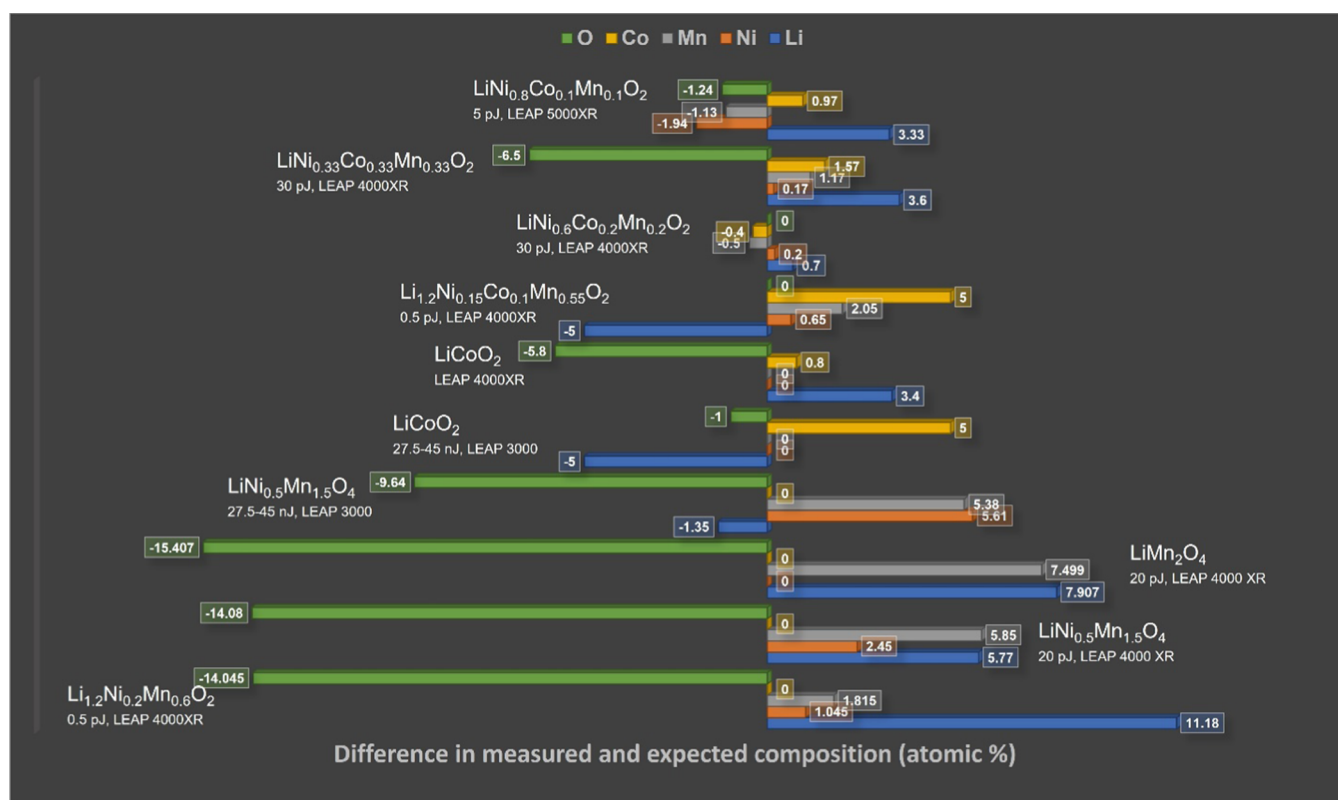
A

Figure 1. Shows the difference in atomic composition (in %) between the expected quantity from the stoichiometry and the observed composition from APT measurement for different battery cathodes. The laser pulse energy used in each case study is also shown.[36−43]

This would help in understanding the penetration levels and surface versus subsurface compositions, as well as identifying Li distribution in nanoscale coatings (of lithium phosphates, fluorides, and oxides) with emphasis on the interface properties.[1]

However, analyzing the distribution of dopants and light elements such as Li within individual battery electrode particles and nanoscale coatings is challenging. Characterization techniques such as (scanning) transmission electron microscopy ((S)TEM), electron energy loss spectrometry (EELS) at room temperature and cryogenic temperatures, and secondary ion mass spectrometry (SIMS) do not provide the combined three-dimensional (3D) sub-nanometer-scale spatial resolution and compositional sensitivity below 1 atom % required to analyze low-atomic-number (Z) elements such as Al and O as well as observe the lithium distribution. The resolution required to analyze cathode secondary particles with graded surface coatings and hence changes in composition from surface to bulk of a ~100 nm sized nanoparticle further complicate this challenge. Atom probe tomography (APT) is one such 3D compositional analysis method that provides both the required sub-nanometer spatial resolution and compositional sensitivity needed to analyze elemental variations within individual battery cathode particles. Hence, for the continuous development of anodes, cathodes, and solid electrolytes for Li-ion batteries, APT continues to play a crucial role in the future. A 3D compositional mapping obtained from APT can further provide answers to the compositional changes (if any) during cycling and the nature of compositional heterogeneity/homogeneity in pristine and cycled electrodes that directly affect the battery electrochemistry.

Compositional quantification of oxide-based materials using APT has been a significant challenge.[15−18] The composition, atomic density, and morphology (for nm sized particles) are all affected by the nature of the high electric fields and pulsed laser applied during APT.[19] To better understand high field evaporation processes, multiple experimental and theoretical investigations have been carried out. Hatzoglou et al.[19] explored the trajectory aberration due to local variations in atomic density and proposed a corrected volume fraction calculation for accurate composition analysis in yttrium titanium oxide. Kirchhofer et al.[20] studied the effect of laser pulse energy and base temperature on the mass resolution, multihit events, and stoichiometry for cerium oxide. To this effect, Valderrama et al.[21] demonstrated an understanding of the influence of instrument parameters for uranium oxide. Mazumder et al.[22] also explained the difference in evaporation processes in the MgO-Fe thin films and bulk MgO films. Devaraj et al.[23] also demonstrated that an APT-measured oxide stoichiometry has a parametric dependence on the laser pulse energy, with oxygen content diminishing at higher laser energies and preferential evaporation of Mg occurring in a pure MgO system.

Digging deeper into the mechanism of field evaporation behavior of oxides, both Devaraj et al.[23] and Karahka et al.[24] used computational methods to explain the stoichiometry effect as either formation of neutral O_2 species or the movement of the O^- away from the tip apex. In addition, using magnetite, Schreiber et al.[25] also demonstrated that post-ionization theory alone could not explain the observed differences in the charge states of Fe in oxides as it does for metallic systems, indicating a closer interplay between the oxygen and the metallic species. Gault et al.[26] provided a detailed review of GaN with DFT simulations to further show that the direct thermal emission of neutral N_2

without ionization is unlikely due to the very high electric fields on the APT specimen apex. An alternative explanation of the occurrence of molecular dissociation and formation of neutrals after field evaporation that could not be detected was provided as more plausible reasoning for stoichiometric changes. Vella et al.[27] used experimental observations on titanium dioxide and magnesium oxide to show that between photoionization and thermal-assisted ionization, the latter is the dominant mechanism for field evaporation of bulk oxides. Moreover, a fast and slow thermal process occurs with a fast lateral cooling of the tip and a slower cooling into the bulk of the specimen tip. Silaeva et al.[28,29] also addressed the theoretical issues of the field evaporation of oxides as occurring due to a combination of different factors: [a] band bending at high electrostatic fields allowing high band gap materials like MgO (7.8 eV) with UV laser wavelengths of 355 nm (5.6 eV), [b] accumulation of holes on the specimen tip surface, [c] photon-assisted tunneling, and [d] presence of lower band gap states to allow field evaporation due to unintentional defect creation during sample preparation. Both the mechanism of surface absorption leading to changes in the band structure and a thermal-assisted effect across the two time scales are also supported by Kelly et al.[30] *Ab initio* calculations by Tsukada et al.[31] as well as Tamura et al.[32] and DFT (density functional theory) by Xia et al.[33] all support the theory of hole accumulation on the specimen surface. Moreover, Karahka et al.[34] also demonstrate *ab initio* results on partial and full band bending for zinc oxide and silicon clusters, respectively. Overall, using a simple single oxide system, a better understanding of the mechanism of field evaporation in oxides and associated thermal effects that occur is provided, which can help explain differences in stoichiometry, mass resolution, and oxygen neutrals and/or migration as a function of APT instrument parameters. Further, to mitigate the thermal effects, Seol et al.[35] also studied the silver capping on MgO bulk films to improve mass resolution.

However, cathodes for lithium-ion batteries are made of four to five elements including oxygen, lithium, and transition metals. In addition, the need for quantitative analysis is stringent as even minor nanoscale structural changes can propagate over cycles and during accelerated testing to cause significant failures. The existing literature on the APT analysis of battery cathodes shows large variations in the experimental composition as compared to expected values from the stoichiometry, an effect that is expected to be more pronounced than the simple oxides discussed above. The bar graph in Figure 1 shows the difference (positive or negative as observed) between the measured composition from APT vs expected composition from stoichiometry as well as the variability in APT laser energies used. Values used to generate the plot are shown in Supporting Information Table S1. Cameca (atom probe tool manufacturer) in conjunction with research institutes also investigated the dependence of laser pulse energy on transition-metal-based cathodes of the Ni−Mn−Co (NMC) type.[36]

While these studies demonstrate the value of APT in 3D nanoscale compositional analysis of battery cathodes, the deviation in the measured composition from expected stoichiometry highlights the need to better understand the parametric effect arising from the APT sample preparation and APT data acquisition parameters. In this direction, a recent work by Kim et al.[44] reveals the dependency of a variety of sample preparation methodologies on the APT results from NMC811 cathodes. Specifically, in the case of samples prepared by cryogenic PFIB and/or ultrahigh vacuum transfer, they reported

the occurrence of an electrostatic field induced by in situ delithiation because of ion migration. Additionally, it was revealed that room-temperature Ga-FIB preparation and atmospheric transfer of NMC811 lead to a beneficial surface modification, helping in shielding the electrostatic field, resulting in the successful APT data analysis. In this work, we further analyze the variations in compositional analysis of Ga-FIB prepared at room temperature and atmospherically transferred NCA-$LiNi_{0.8}Co_{0.15}Al_{0.05}O_2$ Li-ion battery cathode APT samples as a function of APT analysis parameters. We analyze the relationship between the laser pulse energy and the effective electrostatic field (quantified by Ni^{2+}/Ni^{1+} charge−state ratio) and APT-measured composition. The detailed description of the APT mass-to-charge spectra and the compositional variation highlights the need to obtain such APT parametric studies to accurately interpret the APT results from these complex Li-ion battery cathodes.

■ EXPERIMENTAL SECTION

Materials Used. Pristine NCA cathode materials obtained from Toda Materials, with an average particle size between 5 and 10 μm were used for this study. The secondary particles of NCA are shown in Figure 2a. The cathode powders were stored in an
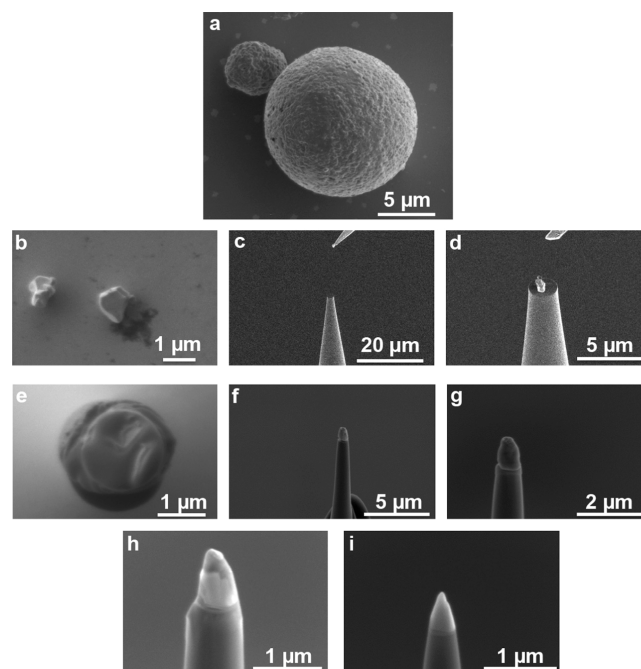

Figure 2. SEM images showing the pristine NCA secondary particle (a) and the steps involved in the APT needle sample preparation right from the primary particles dispersed on a silicon wafer (b) to the end of the final step of low-kV annular milling (i).

Ar-filled glovebox and, in certain cases, transported to Pacific Northwest National Laboratory (PNNL) for APT sample preparation and analysis in a sealed container filled with Ar. In other cases, lift-out sections were transported to PNNL for further specimen preparation.

APT Sample Preparation. To prepare APT needle samples, cathode particles were dispersed on a ~5 by 5 mm piece of Si wafer using a spatula. The as-dispersed particles were then lightly crushed using a clean glass slide to break the secondary particles into individual primary particles shown in Figure 2b.
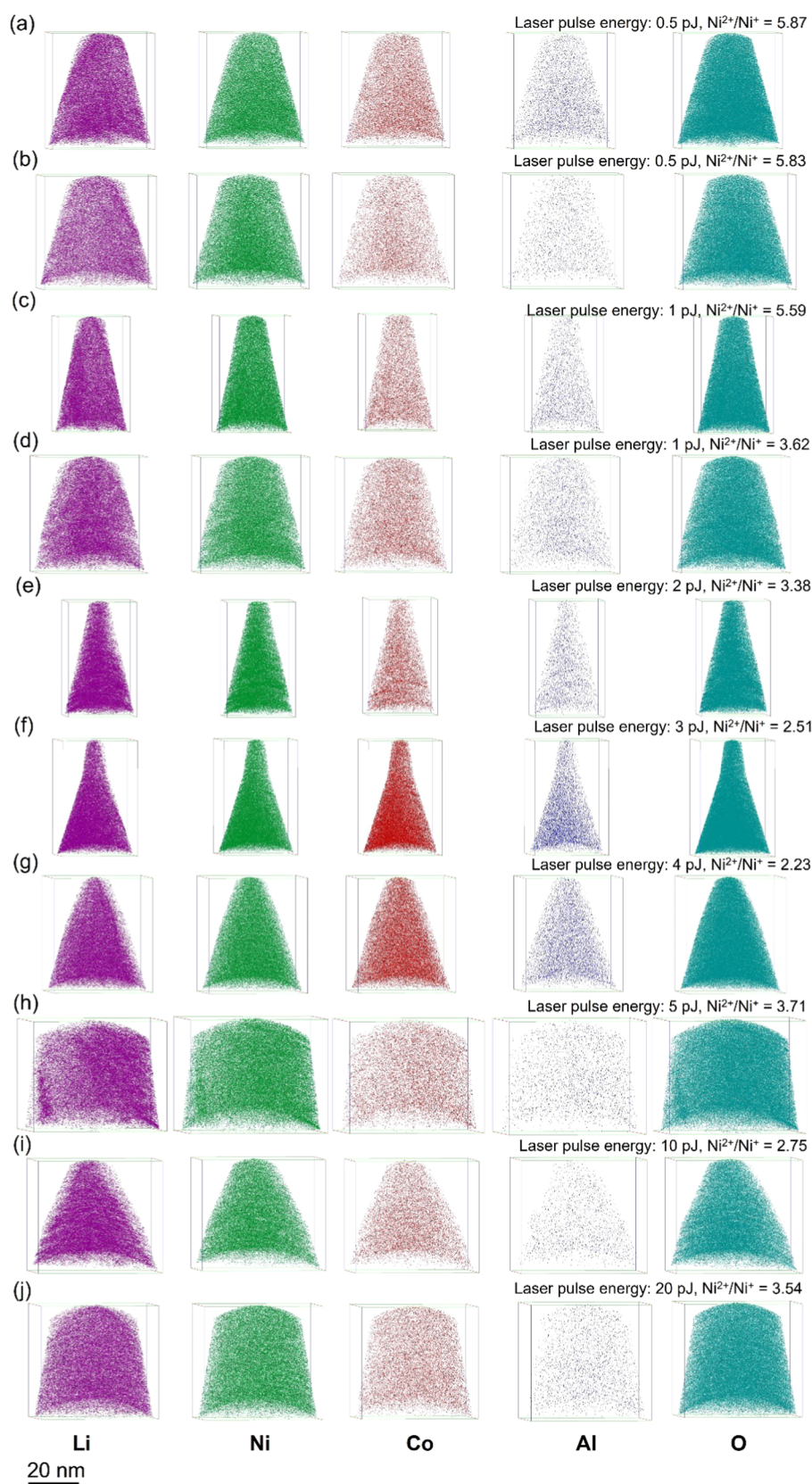
Figure 3. (a–j) Representative ion maps from the APT reconstruction of NCA for Li, Ni, Co, Al, and O. The laser pulse energy used and the charge–state ratios (Ni^{2+}/Ni^+) obtained from the Ni peaks are also shown for each case.

The as-prepared samples were loaded into either the Helios FIB at the Environmental Molecular Sciences Laboratory (EMSL) at PNNL, Richland, WA, or into the Scios at the San

Diego Nanotechnology Infrastructure (SDNI) of UC, San Diego, for further manipulation and APT needle sample preparation. An Omniprobe micromanipulator was used under
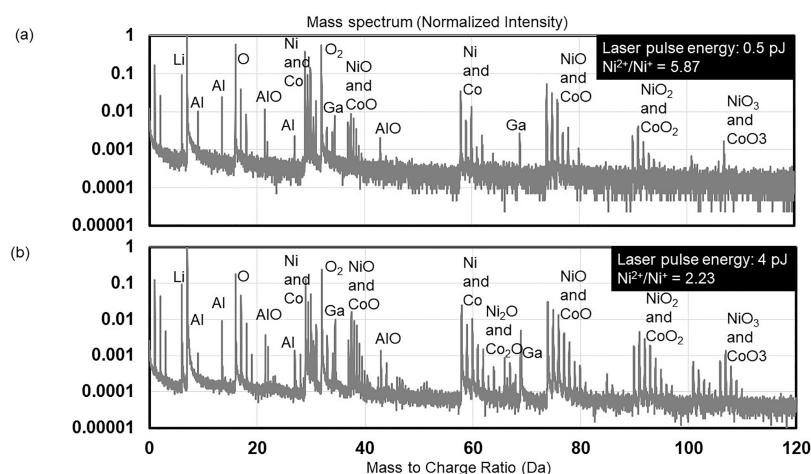
Figure 4. Normalized peak intensity plotted as a function of mass-to-charge ratio for the case of low laser pulse energy (high charge−state ratio) and high laser pulse energy (low charge−state ratio).

electron-beam imaging at a 3 kV accelerating voltage only (no ion-beam imaging) to individually transfer the primary particles (300−500 nm) onto Si microtip array posts. Electrostatic forces between the micromanipulator and the battery cathode particle were leveraged for the manipulation of individual nanoparticles as shown in Figure 2c,d. Subsequently, each particle was coated with a ∼200 nm thick electron-beam-assisted Pt deposition layer, followed by a 500−700 nm thick Ga ion-beam-assisted Pt deposition layer. The diameter of the circular pattern used for the Pt deposition was larger than the particle dimensions to ensure that the particle is encased in Pt. Particles with deposited Pt are shown in Figure 2e.

Following this, annular milling was carried out using a 30 kV and 0.23 nA Ga ion beam, until a needle apex diameter of 800 nm was obtained. 46pA Ga ion-beam current was subsequently used until the diameter was <200 nm. During annular milling, any holes or gaps that appeared between the nanoparticles and the microtip array underneath were filled with the electron-beam-assisted Pt deposition. The final step of annular milling and removal of protective e-beam-deposited Pt was performed using a 2 kV, 24−47 pA Ga ion beam. Using the secondary electron image contrast between NCA and Pt (as seen in Figure 2h), the final step of annular milling was stopped as soon as the needle apex was within the NCA nanoparticle. The final steps of the annular milling process are shown in Figure 2g−i.

APT Experimental Parameters and Analysis. The as-prepared specimens were loaded into the LEAP 4000 XHR at the EMSL at PNNL. The data acquisition was carried out at a base temperature of 40 K and laser pulse energy between 0.5 and 20 pJ with a fixed pulse repetition rate of 125 kHz. A detection rate of 0.005 ions/pulse was used for all runs. The obtained data were reconstructed using CAMECA's IVAS 3.8.6 software.

RESULTS AND DISCUSSIONS

Representative ionic maps for each element from the APT reconstruction of NCA are given in Figure 3. Individual runs with laser energies from 0.5 to 20 pJ are all analyzed and the maps show a homogeneous distribution in the pristine state for Ni, Co, Al, and O. The laser pulse energy and charge−state ratio (Ni^{2+}/Ni^+) for each run is displayed in Figure 3. For the Li maps, areas of nonuniformity or low Li content are associated with Ga damage due to the specimen preparation process (images not shown here). To better understand the Li composition and

uniformity, an iso-concentration surface of 0.5 atomic Ga is chosen, and the low-gradient side is exported for further analysis (see Figures S1 and S2). Frequency distribution analysis shows no statistical significance for the heterogeneous Li distribution for all cases except at 5 pJ (see Supporting Figure S3). Figure 3 also shows a range of charge−state ratios across the different laser pulse energies used.

To ensure that similar peaks are evaporated at different charge−state ratios, the normalized mass-to-charge spectrum at the lowest and highest charge−state ratio is shown in Figure 4. The intensity for each peak is normalized to the highest value for each case separately. At lower laser pulse energy (higher charge−state ratio), the background levels are higher and the lower-intensity oxide peaks for instance NiO_2^+ are less intense (Figure 4a), whereas the same peaks are clearly visible at higher laser pulse energy (lower charge−state ratio) in Figure 4b. Moreover, Li evaporation occurs exclusively as Li^+, whereas other elements evaporate as both elemental species, Al, Ni, Co, and O, and molecular species, AlO, NiO, NiO_2, NiO_3, CoO, CoO_2, and CoO_3, at different charge states. Of specific note is the absence of Li oxide molecular species in the mass-to-charge spectrum. Laser pulse energies over 20 pJ are not investigated due to the nonuniformity in the Li evaporation seen on the detector histogram during run-time, indicating preferential evaporation of Li, which has a low evaporation field (14 V/nm for Li^+). Li uniformity in regions outside of Ga damage is investigated using the binomial distribution for random distribution (Supporting Information Figure S3). The analysis shows a statistically uniform Li distribution for all laser pulse energies except 5 pJ. Overall, through the range of the laser pulse energies investigated, the mass-to-charge spectrum peaks remained rather consistent in this study. Elemental and molecular species are seen in the evaporation in both cases.

To further understand the influence of the laser pulse energy and charge−state ratio on the composition, the atomic % from the stoichiometry is compared to the obtained composition from the APT analysis. The effect of Ga is ruled out by obtaining the composition from the low-gradient side of an exported isosurface of Ga at 0.5 atomic % (additional details in Supporting Information Section 2 and Figure S2). Moreover, peak overlaps are also accounted for by following a peak decomposition analysis using the IVAS software obtained from Cameca. The results are shown in Figure 5a,b. The expected composition for
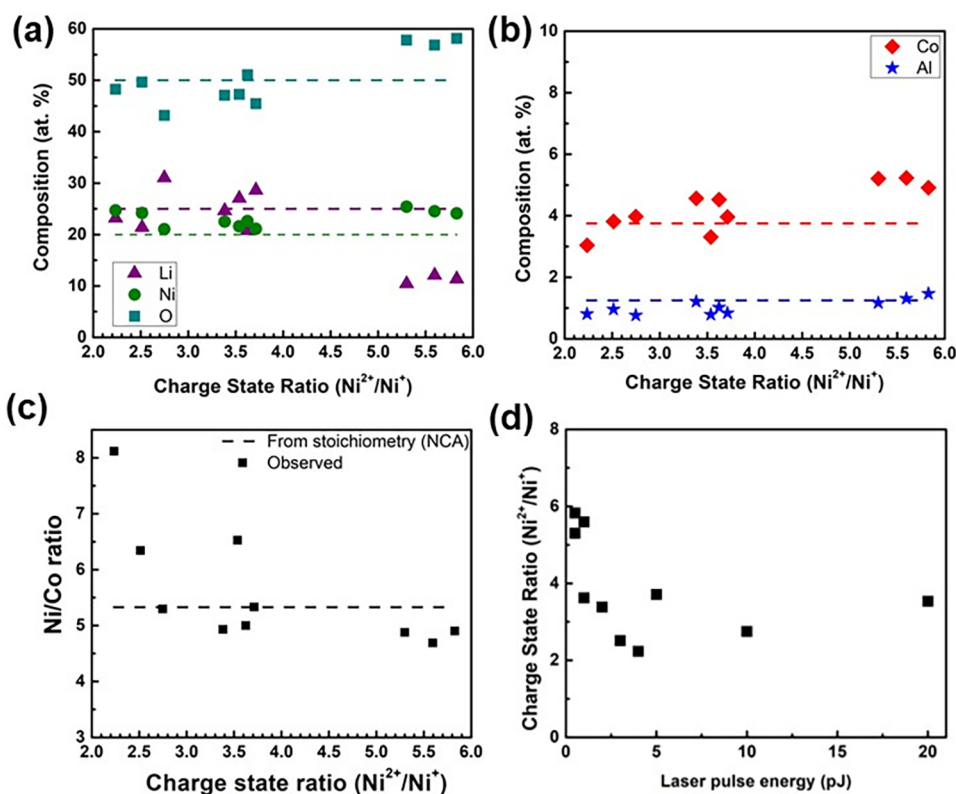
Figure 5. Compositional quantification for NCA at different charge−state ratios, indicative of the laser pulse energy used for Li, Ni, and O (a) and Al and Co (b). The observed Ni/Co ratio, as a metric of accuracy for the Li-ion batteries, is compared with the expected value (dashed line) at different charge−state ratios (c). (d) Charge−state ratio (Ni^{2+}/Ni^+) for each laser pulse energy investigated.

each element is calculated as a ratio of its share in the total stoichiometry; for instance, Li atomic % is 25% since there is one Li in a total of $1 + 0.8 + 0.15 + 0.05 + 2 = 4$ atoms in $LiNi_{0.8}Co_{0.15}Al_{0.05}O_2$. These are plotted as dotted lines in Figure 5a,b. The expected composition is compared with that obtained from APT analysis for all charge−state ratios (calculations used to eliminate any effect from Ga damage and averaging used are reported in Section 2 of the Supporting Information and Table S2). Separate plots are generated for Al and Co since their low atomic % prevents easy viewing of changes in the stoichiometry when combined into one plot. Moreover, the charge−state ratio is used as the x-axis to provide a comparison that is a better representative of the effective electrostatic field on the surface of the specimen.

The atomic compositional analysis in Figure 5a,b follows a trend previously seen for a dependence of the composition on the electric field at the specimen surface. However, a simple decrease in the oxygen content and the increasing composition for Li, Ni, Al, and Co with the increasing charge−state ratio is not seen. On the contrary, for Li, Ni, Co, and O, the composition is more accurately quantified at lower charge−state ratios with a strong deviation at higher charge−state ratios, indicating that the high electric field leads to the underquantification of Li signals and the overquantification of Ni, Co, and O signals. Thus, preferential evaporation can occur at these charge−state ratios (above 4).

Second, the measured Al concentration does not follow the same trend as the other elements, with better quantification at higher charge−state ratios (lower laser pulse energies) above 4. Compared to previous reports,[36,37,43] using the LEAP 4000 tool where higher laser pulse energies (typically indicative of a lower

charge−state ratio) are used for NMC cathodes, our trends for Ni and Co for NCA are in agreement. However, the presence of Al in NCA warrants a closer look at the composition differences coming from the parametric study of the laser pulse energy.

To obtain quantitative results on battery cathodes, the implications and possible explanations for the parametric effect are now discussed. As other parameters, including laser pulse frequency, detection rate, voltage ramp algorithm, and base temperature, are kept fixed for all runs, the effect is attributed to the variation in the effective field at the specimen surface.

An important metric for the battery community is the transition metal ratio, which is studied during various cycling and aging experiments to infer signs of degradation. Deviation from expected ratios could point to the formation of insulating species for cathodes. Figure 5c shows the Ni/Co ratio for NCA. Significant deviations (>50%) at low charge−state ratio are seen.

Moreover, Figure 5d shows the relation between the laser pulse energy and the Ni charge−state ratio. Ultimately, it is clear that the measured composition of all elements is not consistently changing with the charge−state ratio for NCA, indicating that the charge−state ratio alone cannot fully explain the observed phenomenon of the compositional changes.

For the composition analysis, the comparison of the measured composition from Ga-rich and Ga-poor (damage-free) regions is shown in Supporting Information Figure S1. The Ga-rich regions were excluded with total Ga content below 0.5 atomic%. Ga maps and the damaged regions on the Li maps, which are excluded from the composition analysis, are shown in Supporting Information Figure S2.

Thus, having explored and ruled out the obvious choices with the CSR and Ga damage, the explanation for the observed

composition changes due to laser pulse energy would then result from a more complex phenomenon occurring during the field evaporation process. The physics behind high field evaporation of complex oxide is certainly an ongoing topic of interest in the community, and further understanding is needed likely with simulations for a concise explanation. We do not attempt to carry that out here; however, a brief discussion on the contributing factors is presented.

NCA has a band gap close to zero due to the high Ni content that gives it a metal-like nature.[45] This could allow field evaporation at laser pulse energies as low as 0.5 pJ. The change in the measured composition from the APT laser pulse energy (correlated to field strength with the Ni charge−state ratio) can be attributed to the combination of three factors. First, the crystal structure of Li-containing battery oxides likely has a strong influence on the electrostatic fields at the APT needle surface. The HCP (hexagonal close-packed) layered ($R\bar{3}m$) structure consists of alternating layers of Li, O, and Ni/Co/Al, giving rise to an ABC stacking. The differentiating feature is the 2D layers of Li with high ionic mobility. These high Li-ion mobility layers also indicate low bonding energy between the Li and O, which may allow for exclusive elemental evaporation of Li during APT field evaporation. The high Li ionic mobility certainly points to more complex interactions as compared to other simpler oxides, where the ionic mobility of individual species is not high within the lattice. Second, the local change in the bonding environment of each metal ion with oxygen within these layered structures could influence the field evaporation and molecular formation during APT field evaporation.

Overall, a combination of the layered structure typical of lithium-containing battery oxides, the presence of crystallographic planes of high Li mobility, and the local bonding environment of each element within these complex oxide lattices could all play a role in the observed parametric dependence of the composition measured by APT. Our results point to a more complex field evaporation behavior of NCA, which directly affects the APT-measured composition of each element to vary as opposed to simpler oxides like MgO, ZnO, and UO_2 reported in the literature. While band bending, strong optical absorption effects, and hole accumulation on the surface would be expected for the battery cathodes also during APT, given their low band gaps, additional thermal- or photon-assisted mechanisms coupled with mobile species like Li are likely to also influence the field evaporation of these complex oxides with inherently high Li-ion mobilities. To obtain quantitative results, a careful parametric investigation is necessary in the future, with a special focus on understanding molecular fragmentation. Moreover, we observed that accurate quantification of Al versus Ni and Co in battery cathode oxides using APT could be achieved at different laser pulse energies.

CONCLUSIONS

A parametric investigation of the effect of laser pulse energy on the quantitative composition of pristine Ni-rich NCA cathodes was carried out. The analysis indicated that complex oxides containing multiple cationic species would behave differently under a laser-assisted field evaporation process, making a systematic parametric investigation with APT necessary to build an initial understanding of changes in the measured composition as a function of APT analysis parameters. Even under optimized conditions, one single laser pulse energy (and hence the effective electric field) could not give an accurate composition for all elements. Both charge−state ratio and Ga damage were

investigated to show that the observed effect could not be fully explained because of either. For a quantitative analysis of the same battery cathodes before and after cycling using APT, it was hence recommended that analysis conditions were kept consistent, especially, the effective electric field on the APT specimen surface, which was measured as the Ni^{2+}/Ni^{1+} charge−state ratio for the NCA cathode in this work.

ASSOCIATED CONTENT

ⓢ Supporting Information

The Supporting Information is available free of charge at https://pubs.acs.org/doi/10.1021/acs.jpcc.2c01217.

Table S1 contains numbers used to plot Figure 1, Table S2 contains composition numbers used for Figure 5, Figure S1 compares the effect of Ga on the composition analysis in the low-gradient and high-gradient regions, Figure S2 shows the Ga maps for each laser pulse energy, and Figure S3 shows the statistical analysis for Li uniformity (PDF)

AUTHOR INFORMATION

Corresponding Authors

Ying Shirley Meng − *Pritzker School of Molecular Engineering, University of Chicago, Chicago, Illinois 60637, United States; Department of NanoEngineering, University of California San Diego, La Jolla, California 92093, United States;* ⓞ orcid.org/0000-0001-8936-8845; Email: shirleymeng@uchicago.edu

Arun Devaraj − *Physical and Computational Sciences Directorate, Pacific Northwest National Laboratory, Richland, Washington 99354, United States;* ⓞ orcid.org/0000-0003-1314-6212; Email: arun.devaraj@pnnl.gov

Authors

Pritesh Parikh − *Department of NanoEngineering, University of California San Diego, La Jolla, California 92093, United States*

Hyeseung Chung − *Department of NanoEngineering, University of California San Diego, La Jolla, California 92093, United States*

Ethan Vo − *Physical and Computational Sciences Directorate, Pacific Northwest National Laboratory, Richland, Washington 99354, United States*

Abhik Banerjee − *Department of NanoEngineering, University of California San Diego, La Jolla, California 92093, United States; Research Institute for Sustainable Energy (RISE), TCG Centres for Research and Education in Science and Technology (TCG CREST), Salt Lake, Kolkata 700091, India*

Complete contact information is available at:
https://pubs.acs.org/10.1021/acs.jpcc.2c01217

Author Contributions

P.P. conducted the experimental work related to APT sample preparation, data acquisition, and analysis. H.C. provided the pristine NCA electrodes. E.V. supported the data acquisition at Pacific Northwest National Laboratory. A.B. assisted with data interpretation. Y.S.M. and A.D. supervised the research and contributed to the manuscript writing and revision. The manuscript was written through contributions of all authors. All authors have given approval to the final version of the manuscript.

Notes
The authors declare no competing financial interest.

■ REFERENCES

(1) Xin, F.; Zhou, H.; Chen, X.; Zuba, M.; Chernova, N.; Zhou, G.; Whittingham, M. S. Li−Nb−O Coating/Substitution Enhances the Electrochemical Performance of the LiNi0.8Mn0.1Co0.1O2 (NMC 811) Cathode. *ACS Appl. Mater. Interfaces* **2019**, *11*, 34889−34894.

(2) Schipper, F.; Erickson, E. M.; Erk, C.; Shin, J.-Y.; Chesneau, F. F.; Aurbach, D. Review—Recent Advances and Remaining Challenges for Lithium Ion Battery Cathodes I. Nickel-Rich, LiNixCoyMnzO2. *J. Electrochem. Soc.* **2017**, *164*, A6220−A6228.

(3) Liu, H.; Wolf, M.; Karki, K.; Yu, Y.-S.; Stach, E. A.; Cabana, J.; Chapman, K. W.; Chupas, P. J. Intergranular Cracking as a Major Cause of Long-Term Capacity Fading of Layered Cathodes. *Nano Lett.* **2017**, *17*, 3452−3457.

(4) Sun, Y.-K.; Myung, S.-T.; Park, B.-C.; Prakash, J.; Belharouak, I.; Amine, K. High-Energy Cathode Material for Long-Life and Safe Lithium Batteries. *Nat. Mater.* **2009**, *8*, 320−324.

(5) Sallis, S.; Pereira, N.; Mukherjee, P.; Quackenbush, N. F.; Faenza, N.; Schlueter, C.; Lee, T.-L.; Yang, W. L.; Cosandey, F.; Amatucci, G. G.; Piper, L. F. J. Surface Degradation of Li1−XNi0.80Co0.15Al0.05O2 Cathodes: Correlating Charge Transfer Impedance with Surface Phase Transformations. *Appl. Phys. Lett.* **2016**, *108*, No. 263902.

(6) Zhang, H.; Karki, K.; Huang, Y.; Whittingham, M. S.; Stach, E. A.; Zhou, G. Atomic Insight into the Layered/Spinel Phase Transformation in Charged LiNi 0.80 Co 0.15 Al 0.05 O 2 Cathode Particles. *J. Phys. Chem. C* **2017**, *121*, 1421−1430.

(7) Chae, B.-G.; Park, S. Y.; Song, J. H.; Lee, E.; Jeon, W. S. Evolution and Expansion of Li Concentration Gradient during Charge−Discharge Cycling. *Nat. Commun.* **2021**, *12*, No. 3814.

(8) Kim, N. Y.; Yim, T.; Song, J. H.; Yu, J.-S.; Lee, Z. Microstructural Study on Degradation Mechanism of Layered LiNi0.6Co0.2Mn0.2O2 Cathode Materials by Analytical Transmission Electron Microscopy. *J. Power Sources* **2016**, *307*, 641−648.

(9) Jung, S.-K.; Gwon, H.; Hong, J.; Park, K.-Y.; Seo, D.-H.; Kim, H.; Hyun, J.; Yang, W.; Kang, K. Understanding the Degradation Mechanisms of LiNi0.5Co0.2Mn0.3O2 Cathode Material in Lithium Ion Batteries. *Adv. Energy Mater.* **2014**, *4*, No. 1300787.

(10) Takanashi, S.; Abe, Y. Improvement of the Electrochemical Performance of an NCA Positive-Electrode Material of Lithium Ion Battery by Forming an Al-Rich Surface Layer. *Ceram. Int.* **2017**, *43*, 9246−9252.

(11) Mohanty, D.; Dahlberg, K.; King, D. M.; David, L. A.; Sefat, A. S.; Wood, D. L.; Daniel, C.; Dhar, S.; Mahajan, V.; Lee, M.; Albano, F. Modification of Ni-Rich FCG NMC and NCA Cathodes by Atomic Layer Deposition: Preventing Surface Phase Transitions for High-Voltage Lithium-Ion Batteries. *Sci. Rep.* **2016**, *6*, No. 26532.

(12) Hou, P.; Zhang, H.; Deng, X.; Xu, X.; Zhang, L. Stabilizing the Electrode/Electrolyte Interface of LiNi0.8Co0.15Al0.05O2 through Tailoring Aluminum Distribution in Microspheres as Long-Life, High-Rate, and Safe Cathode for Lithium-Ion Batteries. *ACS Appl. Mater. Interfaces* **2017**, *9*, 29643−29653.

(13) Shi, J.-L.; Qi, R.; Zhang, X.-D.; Wang, P.-F.; Fu, W.-G.; Yin, Y.-X.; Xu, J.; Wan, L.-J.; Guo, Y.-G. High-Thermal- and Air-Stability Cathode Material with Concentration-Gradient Buffer for Li-Ion Batteries. *ACS Appl. Mater. Interfaces* **2017**, *9*, 42829−42835.

(14) Qiu, Q.-Q.; Shadike, Z.; Wang, Q.-C.; Yue, X.-Y.; Li, X.-L.; Yuan, S.-S.; Fang, F.; Wu, X.-J.; Hunt, A.; Waluyo, I.; Bak, S.-M.; Yang, X.-Q.; Zhou, Y.-N. Improving the Electrochemical Performance and Structural Stability of the LiNi0.8Co0.15Al0.05O2 Cathode Material at High-Voltage Charging through Ti Substitution. *ACS Appl. Mater. Interfaces* **2019**, *11*, 23213−23221.

(15) *Atom Probe Microscopy*; Gault, B., Ed.; Springer series in materials science; Springer: New York, 2012.

(16) Larson, D. J.; Prosa, T. J.; Ulfig, R. M.; Geiser, B. P.; Kelly, T. F. *Local Electrode Atom Probe Tomography*; Springer New York: New York, NY, 2013. DOI: 10.1007/978-1-4614-8721-0.

(17) Miller, M. K. *Atom-Probe Tomography: The Local Electrode Atom Probe*; Springer: New York, 2014.

(18) Cuduvally, R.; Morris, R. J. H.; Ferrari, P.; Bogdanowicz, J.; Fleischmann, C.; Melkonyan, D.; Vandervorst, W. Potential Sources of Compositional Inaccuracy in the Atom Probe Tomography of InxGa1-XAs. *Ultramicroscopy* **2020**, *210*, No. 112918.

(19) Hatzoglou, C.; Radiguet, B.; Pareige, P. Experimental Artefacts Occurring during Atom Probe Tomography Analysis of Oxide Nanoparticles in Metallic Matrix: Quantification and Correction. *J. Nucl. Mater.* **2017**, *492*, 279−291.

(20) Kirchhofer, R.; Teague, M. C.; Gorman, B. P. Thermal Effects on Mass and Spatial Resolution during Laser Pulse Atom Probe Tomography of Cerium Oxide. *J. Nucl. Mater.* **2013**, *436*, 23−28.

(21) Valderrama, B.; Henderson, H. B.; Gan, J.; Manuel, M. V. Influence of Instrument Conditions on the Evaporation Behavior of Uranium Dioxide with UV Laser-Assisted Atom Probe Tomography. *J. Nucl. Mater.* **2015**, *459*, 37−43.

(22) Mazumder, B.; Vella, A.; Deconihout, B.; Al-Kassab, T. Evaporation Mechanisms of MgO in Laser Assisted Atom Probe Tomography. *Ultramicroscopy* **2011**, *111*, 571−575.

(23) Devaraj, A.; Colby, R.; Hess, W. P.; Perea, D. E.; Thevuthasan, S. Role of Photoexcitation and Field Ionization in the Measurement of Accurate Oxide Stoichiometry by Laser-Assisted Atom Probe Tomography. *J. Phys. Chem. Lett.* **2013**, *4*, 993−998.

(24) Karahka, M.; Kreuzer, H. J. Field Evaporation of Oxides: A Theoretical Study. *Ultramicroscopy* **2013**, *132*, 54−59.

(25) Schreiber, D. K.; Chiaramonti, A. N.; Gordon, L. M.; Kruska, K. Applicability of Post-Ionization Theory to Laser-Assisted Field Evaporation of Magnetite. *Appl. Phys. Lett.* **2014**, *105*, No. 244106.

(26) Gault, B.; Saxey, D. W.; Ashton, M. W.; Sinnott, S. B.; Chiaramonti, A. N.; Moody, M. P.; Schreiber, D. K. Behavior of Molecules and Molecular Ions near a Field Emitter. *New J. Phys.* **2016**, *18*, No. 033031.

(27) Vella, A.; Mazumder, B.; Da Costa, G.; Deconihout, B. Field Evaporation Mechanism of Bulk Oxides under Ultra Fast Laser Illumination. *J. Appl. Phys.* **2011**, *110*, No. 044321.

(28) Silaeva, E. P.; Karahka, M.; Kreuzer, H. J. Atom Probe Tomography and Field Evaporation of Insulators and Semiconductors: Theoretical Issues. *Curr. Opin. Solid State Mater. Sci.* **2013**, *17*, 211−216.

(29) Silaeva, E. P.; Vella, A.; Sevelin-Radiguet, N.; Martel, G.; Deconihout, B.; Itina, T. E. Ultrafast Laser-Triggered Field Ion Emission from Semiconductor Tips. *New J. Phys.* **2012**, *14*, No. 113026.

(30) Kelly, T. F.; Vella, A.; Bunton, J. H.; Houard, J.; Silaeva, E. P.; Bogdanowicz, J.; Vandervorst, W. Laser Pulsing of Field Evaporation in Atom Probe Tomography. *Curr. Opin. Solid State Mater. Sci.* **2014**, *18*, 81−89.

(31) Tsukada, M.; Tamura, H.; McKenna, K. P.; Shluger, A. L.; Chen, Y. M.; Ohkubo, T.; Hono, K. Mechanism of Laser Assisted Field

Evaporation from Insulating Oxides. *Ultramicroscopy* **2011**, *111*, 567−570.

(32) Tamura, H.; Tsukada, M.; McKenna, K. P.; Shluger, A. L.; Ohkubo, T.; Hono, K. Laser-Assisted Field Evaporation from Insulators Triggered by Photoinduced Hole Accumulation. *Phys. Rev. B* **2012**, *86*, No. 195430.

(33) Xia, Y. Hole Accumulation Effect on Laser-Assisted Field Evaporation of Insulators. *Ultramicroscopy* **2019**, *196*, 121−128.

(34) Karahka, M.; Kreuzer, H. J. Field Evaporation of Insulators and Semiconductors: Theoretical Insights for ZnO. *Ultramicroscopy* **2015**, *159*, 156−161.

(35) Seol, J.-B.; Kwak, C.-M.; Kim, Y.-T.; Park, C.-G. Understanding of the Field Evaporation of Surface Modified Oxide Materials through Transmission Electron Microscopy and Atom Probe Tomography. *Appl. Surf. Sci.* **2016**, *368*, 368−377.

(36) Lee, J. Y.; Kim, J. Y.; Cho, H. I.; Lee, C. H.; Kim, H. S.; Lee, S. U.; Prosa, T. J.; Larson, D. J.; Yu, T. H.; Ahn, J.-P. Three-Dimensional Evaluation of Compositional and Structural Changes in Cycled LiNi1/3Co1/3Mn1/3O2 by Atom Probe Tomography. *J. Power Sources* **2018**, *379*, 160−166.

(37) Choi, S.; Yun, B.-N.; Jung, W. D.; Kim, T. H.; Chung, K.-Y.; Son, J.-W.; Sang, B.-I.; Jung, H.-G.; Kim, H. Tomographical Analysis of Electrochemical Lithiation and Delithiation of LiNi0.6Co0.2Mn0.2O2 Cathodes in All-Solid-State Batteries. *Scr. Mater.* **2019**, *165*, 10−14.

(38) Mohanty, D.; Mazumder, B.; Devaraj, A.; Sefat, A. S.; Huq, A.; David, L. A.; Payzant, E. A.; Li, J.; Wood, D. L.; Daniel, C. Resolving the Degradation Pathways in High-Voltage Oxides for High-Energy-Density Lithium-Ion Batteries; Alternation in Chemistry, Composition and Crystal Structures. *Nano Energy* **2017**, *36*, 76−84.

(39) Schmitz, G.; Abouzari, R.; Berkemeier, F.; Gallasch, T.; Greiwe, G.; Stockhoff, T.; Wunde, F. Nanoanalysis and Ion Conductivity of Thin Film Battery Materials. *Z. Phys. Chem.* **2010**, *224*, 1795−1829.

(40) Diercks, D. R.; Musselman, M.; Morgenstern, A.; Wilson, T.; Kumar, M.; Smith, K.; Kawase, M.; Gorman, B. P.; Eberhart, M.; Packard, C. E. Evidence for Anisotropic Mechanical Behavior and Nanoscale Chemical Heterogeneity in Cycled LiCoO2. *J. Electrochem. Soc.* **2014**, *161*, F3039−F3045.

(41) Pfeiffer, B.; Maier, J.; Arlt, J.; Nowak, C. In Situ Atom Probe Deintercalation of Lithium-Manganese-Oxide. *Microsc. Microanal.* **2017**, *23*, 314−320.

(42) Maier, J.; Pfeiffer, B.; Volkert, C. A.; Nowak, C. Three-Dimensional Microstructural Characterization of Lithium Manganese Oxide with Atom Probe Tomography. *Energy Technol.* **2016**, *4*, 1565−1574.

(43) Devaraj, A.; Gu, M.; Colby, R.; Yan, P.; Wang, C. M.; Zheng, J. M.; Xiao, J.; Genc, A.; Zhang, J. G.; Belharouak, I.; Wang, D.; Amine, K.; Thevuthasan, S. Visualizing Nanoscale 3D Compositional Fluctuation of Lithium in Advanced Lithium-Ion Battery Cathodes. *Nat. Commun.* **2015**, *6*, No. 8014.

(44) Kim, S.-H.; Antonov, S.; Zhou, X.; Stephenson, L. T.; Jung, C.; El-Zoka, A. A.; Schreiber, D. K.; Conroy, M.; Gault, B. Atom Probe Analysis of Electrode Materials for Li-Ion Batteries: Challenges and Ways Forward. *J. Mater. Chem. A* **2022**, *10*, 4926−4935.

(45) Sun, H.; Zhao, K. Electronic Structure and Comparative Properties of LiNi$_x$Mn$_y$Co$_z$O$_2$ Cathode Materials. *J. Phys. Chem. C* **2017**, *121*, 6002−6010.